Electronic Supplementary Material (ESI) for Soft Matter.

Supporting Information for Energetically favoured defects in dense packings of particles on spherical surfaces

Stefan Paquay[1], Halim Kusumaatmaja[2], David J. Wales[3], Roya Zandi[4], and Paul van der Schoot[1,5]

[1]Department of Applied Physics, Technische Universiteit Eindhoven, The Netherlands

[2]Department of Physics, University of Durham, UK

[3]Department of Chemistry, University of Cambridge, UK

[4]Department of Physics and Astronomy, University of California, Riverside, USA

[5]Instituut voor Theoretische Fysica, Universiteit Utrecht, The Netherlands

S 1 Optimal sphere radius and energy

In this section we present our results for the optimal sphere radius R^* and the corresponding energies that are described in Section 2. We also show the optimal Lennard-Jones radii and energies reported by Voogd in (1). They are located in Tab. S 1. Our values are obtained from simulations in which the radius of the spherical template slowly shrinks over a range estimated from hard disk packings in 2D that presumably contains the optimal radius. Note that our

radii for the Lennard-Jones packing do not improve upon Voogd's values, they are in the correct ballpark, with the largest difference in the radius being 2%. Thus, our strategy provides a good way to obtain a first order estimate for the optimal radius on which more intensive optimisation can be performed.

Table S 1: Optimal radii and corresponding potential energy for Lennard-Jones particles and Morse particles with shape parameter $\alpha = 60/r_0$, where r_0 is the distance at which the pair potential has its minimum.

N	R^*_{LJ}/r_0	$U_{LJ}/N/\epsilon$	R^*_{LJ}/r_0 (Voogd)	$U_{LJ}/N/\epsilon$ (Voogd)	R^*_M/r_0	$U^*_M/N/\epsilon$
10	0.904877	-2.386829	0.897777352534	-2.391701447066	0.951257	-2.099895
11	0.940335	-2.546418	0.940905005832	-2.546447320801	0.950446	-2.268700
12	0.936682	-2.795960	0.942373155294	-2.799795573727	0.951435	-2.498530
13	1.022253	-2.448824	1.023669635577	-2.448969977079	1.090487	-1.966043
14	1.051020	-2.532894	1.053553039689	-2.533348412369	1.070727	-1.999874
15	1.077747	-2.604019	1.079511939730	-2.604254157791	1.107120	-1.996530
16	1.113089	-2.629181	1.111359350373	-2.629397082119	1.135076	-1.997704
17	1.136519	-2.729079	1.134715561189	-2.729322104280	1.177153	-2.108171
18	1.169474	-2.720606	1.168431468281	-2.720681589556	1.192575	-2.143180
19	1.212959	-2.692581	1.212803380000	-2.692582368658	1.246011	-2.162748
20	1.220995	-2.812968	1.221102153780	-2.812968910809	1.243276	-2.238600
21	1.263170	-2.759161	1.256842828104	-2.761570772616	1.290012	-2.033690
22	1.280587	-2.813962	1.278935841127	-2.814127147712	1.345578	-2.309422
23	1.321960	-2.798679	1.323636299622	-2.798822415653	1.344108	-2.390687
24	1.337533	-2.916111	1.325942483975	-2.923589586974	1.343885	-2.499904
25	1.365106	-2.789403	1.370215612837	-2.790744681095	1.409161	-2.143061
26	1.405526	-2.831581	1.393253846649	-2.838736266635	1.426258	-2.064923
27	1.405019	-2.915403	1.405226921913	-2.915404947140	1.438392	-2.174199
28	1.444699	-2.834263	1.441037402745	-2.834795918128	1.486233	-2.109257
29	1.470268	-2.836935	1.470703678855	-2.836943974529	1.506661	-2.157828
30	1.481021	-2.907705	1.482942826361	-2.907879985814	1.512497	-2.264060

Continued on next page

Table S 1 – *Continued from previous page*

N	R^*_{LJ}/r_0	$U_{LJ}/N/\epsilon$	R^*_{LJ}/r_0 (Voogd)	$U_{LJ}/N/\epsilon$ (Voogd)	R^*_M/r_0	$U^*_M/N/\epsilon$
31	1.505503	-2.914502	1.508252602796	-2.914845518606	1.569113	-2.171004
32	1.529593	-2.973958	1.517799565208	-2.980094374797	1.556748	-2.156241
33	1.553309	-2.851437	1.565483089900	-2.857364512086	1.607324	-2.090012
34	1.576668	-2.879003	1.581507917153	-2.879973993426	1.663424	-2.215261
35	1.615217	-2.892769	1.603568457619	-2.897476940815	1.650354	-2.254401
36	1.622380	-2.926064	1.621869926831	-2.926074652855	1.651993	-2.304795
37	1.660724	-2.902360	1.645689466050	-2.907674813755	1.689376	-2.167760
38	1.666836	-2.970314	1.659845132456	-2.972138629420	1.734758	-2.155274
39	1.688627	-2.913506	1.689160940137	-2.913516422414	1.736032	-2.163549
40	1.710142	-2.935197	1.708230437867	-2.935326506885	1.752469	-2.195959
41	1.731381	-2.929093	1.729343588049	-2.929234832467	1.774234	-2.146127
42	1.752371	-2.957193	1.752712826656	-2.957197169053	1.809763	-2.265107
43	1.773111	-2.985056	1.765631923177	-2.986878602028	1.809023	-2.237259
44	1.776194	-3.038971	1.773591356738	-3.039204045422	1.813941	-2.271814
45	1.796266	-2.988776	1.801077961986	-2.989550533032	1.882977	-2.388847
46	1.833924	-2.967809	1.831567835991	-2.967979946789	1.873818	-2.265579
47	1.835750	-2.988661	1.845624666183	-2.991666695750	1.883939	-2.442927
48	1.855172	-3.043492	1.852527998434	-3.043710551686	1.884393	-2.498348
49	1.892777	-2.959511	1.884936044669	-2.961259366808	1.937731	-2.177288
50	1.893427	-2.983355	1.899868057549	-2.984583094281	1.947870	-2.204567
51	1.912270	-2.991444	1.916517435225	-2.991978366226	1.974846	-2.198855
52	1.949857	-2.984952	1.937974048925	-2.988779822952	1.984468	-2.187915
53	1.949402	-2.970368	1.961895379520	-2.974816531472	2.009351	-2.195769
54	1.967710	-3.007974	1.971909776092	-3.008467736524	2.016416	-2.273019
55	2.005315	-2.972047	1.997949144047	-2.973425131693	2.052942	-2.222675
56	2.003818	-3.005524	2.007994951024	-3.005994640032	2.056417	-2.243726
57	2.021627	-2.993537	2.027327589626	-2.994392848924	2.081772	-2.257658

Continued on next page

Table S 1 – *Continued from previous page*

N	R^*_{LJ}/r_0	$U_{LJ}/N/\epsilon$	R^*_{LJ}/r_0 (Voogd)	$U_{LJ}/N/\epsilon$ (Voogd)	R^*_M/r_0	$U^*_M/N/\epsilon$
58	2.059277	-2.991903	2.044677513303	-2.997051140312	2.099946	-2.252599
59	2.056791	-3.009671	2.060451925427	-3.010013049113	2.116954	-2.302388
60	2.074146	-3.032748	2.072914876984	-3.032786493941	2.127555	-2.282841
61	2.091367	-3.004137	2.099984988857	-3.005979486010	2.156723	-2.251880
62	2.108437	-3.021133	2.109459052546	-3.021158756038	2.165891	-2.216732
63	2.125373	-3.022027	2.125802560541	-3.022031670944	2.181170	-2.228638
64	2.142175	-3.020690	2.143018548376	-3.020706178561	2.203763	-2.233371
65	2.180011	-3.014365	2.159849647419	-3.023038735530	2.218712	-2.252606
66	2.175388	-3.034738	2.173766775635	-3.034797798662	2.228147	-2.242949
67	2.191807	-3.033152	2.190095552387	-3.033218086182	2.257012	-2.223577
68	2.229750	-3.009600	2.212957714507	-3.015064415231	2.269333	-2.223757
69	2.224280	-3.034493	2.221952321872	-3.034610208058	2.279338	-2.228245
70	2.240334	-3.042208	2.236128944654	-3.042587333370	2.296906	-2.255365
71	2.256281	-3.047856	2.253609149146	-3.048006785146	2.317771	-2.299356
72	2.272121	-3.056438	2.264321813954	-3.057702042394	2.316996	-2.325058
73	2.287837	-3.019305	2.292383040075	-3.019407304510	2.352293	-2.226592
74	2.303454	-3.030862	2.303497514639	-3.030862374611	2.366227	-2.242038
75	2.318974	-3.044339	2.315406949106	-3.044593521226	2.375216	-2.212863
76	2.334377	-3.043228	2.332264011995	-3.043315920487	2.395653	-2.245938
77	2.349683	-3.051799	2.342682708578	-3.052751366791	2.405489	-2.261926
78	2.364891	-3.067158	2.355651081550	-3.068799176877	2.410416	-2.237785
79	2.380009	-3.046926	2.373368483194	-3.047756931955	2.447245	-2.252494
80	2.395021	-3.053943	2.387441437503	-3.055012900626	2.449508	-1.902176
81	2.409943	-3.040082	2.405496835696	-3.040443111613	2.470801	-2.195361
82	2.424777	-3.036470	2.421820588972	-3.036629161026	2.492485	-2.259488
83	2.439512	-3.039338	2.434795696871	-3.039736810517	2.501109	-2.328417
84	2.454168	-3.051290	2.448182481981	-3.051926932936	2.500183	-2.345918

Continued on next page

Table S 1 – *Continued from previous page*

N	R^*_{LJ}/r_0	$U_{LJ}/N/\epsilon$	R^*_{LJ}/r_0 (Voogd)	$U_{LJ}/N/\epsilon$ (Voogd)	R^*_M/r_0	$U^*_M/N/\epsilon$
85	2.468734	-3.041139	2.464409004970	-3.041467105409	2.529841	-2.209913
86	2.483211	-3.044077	2.478604188594	-3.044445037863	2.544674	-2.224230
87	2.497608	-3.048261	2.493077153951	-3.048615801156	2.555677	-2.204192
88	2.511916	-3.058038	2.504241465416	-3.059034645237	2.571579	-2.265073
89	2.526152	-3.053892	2.519344738182	-3.054668510385	2.582359	-2.252085
90	2.540300	-3.049875	2.540613112184	-3.049877137472	2.606983	-2.251916
91	2.554376	-3.052519	2.551677109091	-3.052638760612	2.617603	-2.210665
92	2.568372	-3.067097	2.559448724569	-3.068391387274	2.616534	-2.281080
93	2.582297	-3.061326	2.578325483646	-3.061580134667	2.644918	-2.250411
94	2.596141	-3.069246	2.588610373792	-3.070146514964	2.651315	-2.127731
95	2.609915	-3.070577	2.600111381806	-3.072084399989	2.669293	-2.297233
96	2.623617	-3.078376	2.609596703568	-3.081425625804	2.678059	-2.287996
97	2.637247	-3.074433	2.626721288869	-3.076135067207	2.695931	-2.298052
98	2.650807	-3.087128	2.635565739021	-3.090663894976	2.697864	-2.282845
99	2.664295	-3.066456	2.653858334618	-3.068095087771	2.727576	-2.205642
100	2.677712	-3.072264	2.663546522523	-3.075249310690	2.743986	-2.232190

S 2 Problems associated with Voronoi tessellation

In a 3D Voronoi construction, the entire simulation volume V is divided into N polyhedra with volume V_i, one for each particle $i = 1, ..., N$ (a Voronoi tessellation). Each volume V_i consists of all points $\mathbf{x}$ that are closer to the position of particle $\mathbf{x}_i$ than to any other particle. Although our particles only have access to a two-dimensional subspace of $\mathbb{R}^3$, they live in a three-dimensional Cartesian space, so it is still possible to assign the aforementioned volumes to

them. The number of faces of each polyhedron is then the number of nearest neighbours of each particle, and a connectivity network can be generated by connecting all particles whose polyhedra share a face.

The network generated by the tessellation covers the entire space, and thus automatically has the correct Euler characteristic. For particles on a sphere, one should generate the equivalent of the three-dimensional Voronoi tesselation on the spherical surface. This can be done by determining the convex hull of the points (2), for which we employ the CGAL software library. (3) This produces a partitioning of the sphere surface where again each point is assigned to the particle that is closest to in geodesic sense.

Such a construction is very natural for hexagonal lattices, as the generated polyhedra are hexagons as well, and they are fairly robust against thermal fluctuations. An issue arises when particles are packed in other types of lattice, however. For example, in a perfectly square lattice, the Voronoi tessellation is degenerate because the cubes around the particles have touching edges and vertices. A small thermal fluctuation will generate an additional face in two of the polyhedra, resulting in either one pair or the other being counted as neighbours, even though the packing should be considered square instead of hexagonal.(4) Based on previous works (5, 6) we anticipated such problems and hence opted for the distance criterion instead.

We present here Fig. S 1 as a clear illustration of a packing for which the Voronoi construction is degenerate. It is an octahedral (7) packing of Lennard-Jones particles that corresponds to the global minimum for $N = 24$, where we colour the coordination of the particles according to the Voronoi tessellation and the distance criterion. Each particle in the packing plays an equivalent role, as they are all at the corner of a square arrangement and touch five other particles. Nevertheless, the Voronoi construction arbitrarily assigns six nearest neighbours to some of the particles. Hence, the Voronoi construction *incorrectly* assigns 12 defects instead of 24 to this packing. This would as a result imply that the packing has no defects at all, which is clearly incorrect as *all* particles

are five-fold defects.

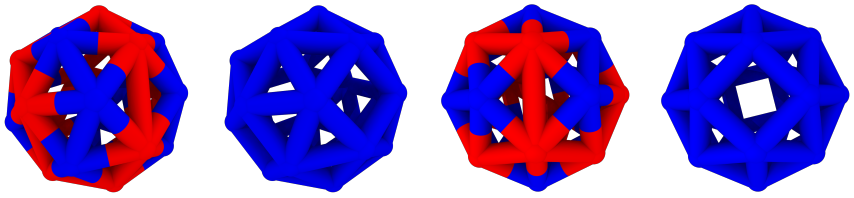

(a) convex hull (a) distance (b) convex hull (b) distance

Figure S 1: (Colour online.) Global potential energy minimum for $N = 24$ Lennard-Jones particles, shown from two vantage points (a) and (b), obtained using the GMIN program.(8) The colour indicates the number of nearest neighbours. Red particles have 6 and blue 5 nearest neighbours, as identified by the convex hull and the distance criterion.

Despite the aforementioned deficiencies of the Voronoi tessellation, it is commonly used in the literature to quantify defects. Therefore, we do present a short analysis of Voronoi tessellation here to allow for easier comparison with said literature. In Fig. S 2 we show the excess defect fraction obtained from the convex hull with the software library CGAL (3). Similar to the distance criterion, we again find that for certain particle numbers, excess defects appear at zero temperature, disappear at intermediate temperatures, then reappear at higher temperatures. This observation suggests that our findings are indeed robust. However, details of the excess defect landscapes calculated from the two methods do vary quite significantly.

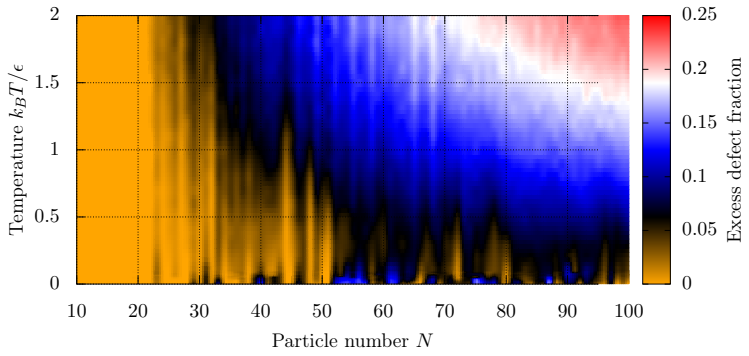

Figure S 2: (Colour online.) Excess defect fraction for $N = 10$ to $N = 100$ Lennard-Jones particles determined by means of the convex hull.

For the distance criterion the number of excess defects for a given temperature does not seem to follow a clear trend as a function of the number of particles. However, for the Voronoi tesselations we see a gradual increase in the number of excess defects with increasing N at fixed temperatures $T > 1\ \epsilon/k_B$. Furthermore, the total number of excess defects in this construction is significantly smaller over the entire temperature range, because of the previously mentioned deficiencies.

For the Voronoi tesselation the largest excess defect fraction is only 0.25, whereas that for the distance criterion it is about 0.8. This difference is explained by the fact that at high temperatures, the particles are effectively a liquid and there are large fluctuations in inter-particle distances. These large fluctuations lead to a considerable fraction of particles that have other than six nearest neighbours. The convex hull is not sensitive at all to the inter-particle distance, and thus does not reach these large values.

S 3 Cut-off radii for distance criterion

In this section we present the cut-off radii we used for the nearest neighbour distance criterion. The distances r^* are chosen to coincide with the minimum after the first peak in the pair distribution function. For those particle numbers N where the first peak was split, we chose r^* so that both split peaks are within r^*. They are tabulated in Tab. S 2.

Table S 2: Cut-off radii used for the distance neighbour criterion for Lennard-Jones particles and Morse particles with shape parameter $\alpha = 60/r_0$, where r_0 is the distance at which the pair potential has its minimum.

N	r^* (LJ)	r^* (Morse)	N	r^* (LJ)	r^* (Morse)
10	1.1522287	1.1403504	11	1.1284720	1.1997439
12	1.0750181	1.0809568	13	1.1819259	1.0809568
14	1.3500679	1.1522287	15	1.3500679	1.0809568

Continued on next page

Table S 2 – *Continued from previous page*

N	r^* (LJ)	r^* (Morse)	N	r^* (LJ)	r^* (Morse)
16	1.1700467	1.1284720	17	1.0987748	1.0809568
18	1.0631388	1.0809568	19	1.1047144	1.0928361
20	1.0572001	1.0809568	21	1.1759863	1.0809568
22	1.0572001	1.0809568	23	1.2235006	1.0809568
24	1.2710158	1.0809568	25	1.1225324	1.1165928
26	1.1581683	1.1225324	27	1.1878647	1.0868964
28	1.2472582	1.0393821	29	1.1759863	1.0928361
30	1.1581683	1.1225324	31	1.3363481	1.1106540
32	1.3363481	1.2472582	33	1.1938043	1.1938043
34	1.1522287	1.0809568	35	1.1344107	1.1165928
36	1.0809568	1.1759863	37	1.1700467	1.0809568
38	1.1700467	1.0809568	39	1.1581683	1.1581683
40	1.1819259	1.1522287	41	1.1700467	1.1848953
42	1.1700467	1.0809568	43	1.2472582	1.1938043
44	1.3363481	1.2472582	45	1.1284720	1.2472582
46	1.1819259	1.1670773	47	1.0928361	1.2650762
48	1.3363481	1.2650762	49	1.2531978	1.2235006
50	1.1284711	1.2205312	51	1.1700467	1.2472582
52	1.1819259	1.1165928	53	1.1462900	1.2472582
54	1.1581683	1.1522260	55	1.1641080	1.1522260
56	1.1759863	1.1670773	57	1.1819259	1.1938043
58	1.1403504	1.2383492	59	1.1641080	1.2472582
60	1.2353799	1.2472582	61	1.2591366	1.2205312
62	1.1878647	1.1938043	63	1.2116223	1.2472582
64	1.2413186	1.1848953	65	1.2710158	1.2650762
66	1.0750181	1.2160768	67	1.2413186	1.1938043
68	1.2650762	1.2027133	69	1.2116223	1.1938043

Continued on next page

Table S 2 – *Continued from previous page*

N	r^* (LJ)	r^* (Morse)	N	r^* (LJ)	r^* (Morse)
70	1.2472582	1.2294402	71	1.2472582	1.1938043
72	1.2918031	1.2027133	73	1.1700467	1.2116223
74	1.1641080	1.1635137	75	1.1641080	1.1848953
76	1.2027133	1.2116223	77	1.2413186	1.2135822
78	1.0868964	1.1670773	79	1.1522287	1.1848953
80	1.1670773	1.2160768	81	1.2591366	1.2918031
82	1.1700467	1.2027133	83	1.1700467	1.2828942
84	1.1047144	1.2739852	85	1.1759863	1.3363481
86	1.2413186	1.2472582	87	1.1165928	1.2472582
88	1.1047144	1.2472582	89	1.2175619	1.1492593
90	1.1047144	1.2561672	91	1.2591366	1.2561672
92	1.1938043	1.2294402	93	1.1909445	1.2561672
94	1.1878647	1.2650762	95	1.1759863	1.2294402
96	1.2531978	1.1581683	97	1.2531978	1.2472582
98	1.1789441	1.2294402	99	1.2472582	1.2353790
100	1.2365407	1.2472582			

S 4 Additional figures of particle fractions

This section contains additional figures of particle and defect fractions for the Lennard-Jones and Morse packings. In Fig. S 3 we show the fraction of particles with 7 nearest neighbours, revealing that for a Lennard-Jones potential, exciting seven-fold defects thermally is difficult. The largest fraction of seven-fold particles is about 0.018 for 48 particles at $T = 2\epsilon/k_B$.

In Figs. S 4, S 5 and S 6 we show the fraction of particles with three, four and seven nearest neighbours, respectively. Figs. S 4 and S 5 reveal that for

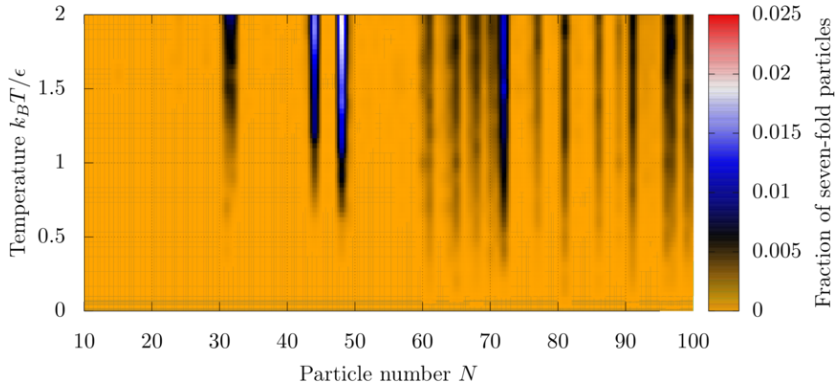

Figure S 3: Fraction of particles with seven nearest neighbours for a Lennard-Jones potential.

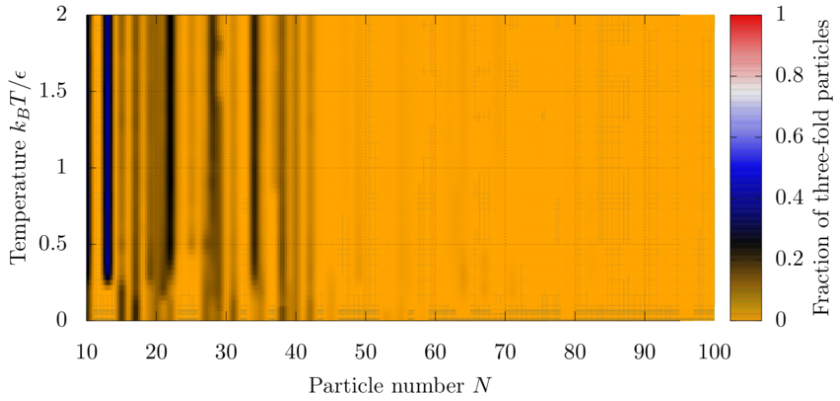

Figure S 4: Fraction of particles with three nearest neighbours for a Morse potential with $\alpha = 60/r_0$.

the sharp Morse potential, there is a significant number of particles with three or four nearest neighbours for smaller particle numbers. This is because for this potential, repulsion drives the optimal packings to lower density, which in turn leads to fewer contacts between the particles. This is also evident from the optimal radii for $N = 11, 12$ and 13 particles, since the optimal radius for 12 is smaller than that for 11 and 13 particles.

S 5 Free energies of packings

This section contains detailed descriptions related to the identification of the packings considered in Section 4. To accurately identify the equilibrium pack-

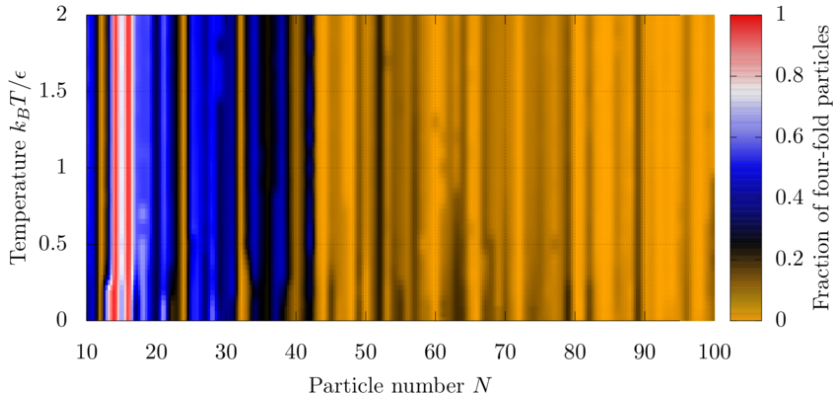

Figure S 5: Fraction of particles with four nearest neighbours for a Morse potential with $\alpha = 60/r_0$.

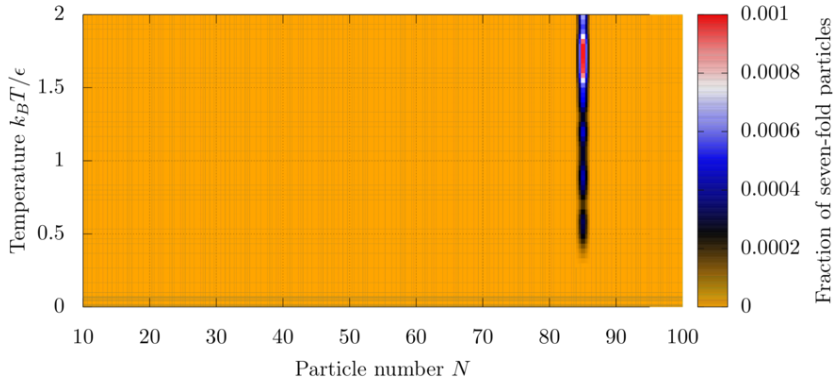

Figure S 6: Fraction of particles with seven nearest neighbours for a Morse potential with $\alpha = 60/r_0$.

ing, we average the particle positions over a short time window to average out fast thermal fluctuations. In particular, we average 250 frames 10 time steps apart, which corresponds to time intervals of $0.05\tau_L$ apart, where τ_L is the Langevin damping time. This averaging is performed every 2500 time steps, which corresponds to intervals of $12.5\tau_L$.

For each of these averaged snapshots, we determine the number of nearest neighbours of each particle according to the neighbour criterion with $r^* = 1.2918031r_0$. For each of these defects, we determine if they are in a defect cluster, where a cluster is defined as all defects that are direct or indirect neighbours of each other. From that information, one can already deduce if the packing is icosahedral, D_{5h}, or D_3, since an icosahedral packing contains twelve defect

clusters of one defect each, the D_{5h} contains five clusters of six defects and two of one defect, and the D_3 packing contains six clusters of one defect and three clusters of six particles.

For additional verification, we determine the root mean square deviation (RMSD) of the particle positions of these snapshots with respect to the identified packing. We do so by assigning to each packing type two axes that are easily obtained from the defect locations. For the D_{5h}, the first axis is the location of the single five-fold defect and the second axis is the average position of the five-fold defects in the cluster of six. For the D_3, the main axis is the average position of the three single five-fold defects on the same side of the three clusters of six defects, and the second axis is the average position of one of those clusters of six. For the icosahedral packing, we take as main axis the position of a single five-fold defect and as second axis another defect that makes an angle of $63.435°$. Because of fluctuations, we iterate over all vertices and find the pair that deviates the least from this fixed angle. For all packings, we make the axes orthonormal using the Gram-Schmidt procedure.

To extract the RMSD, we first identify the packing based on the defect pattern. Then we find the two axes for the packing as well as the reference packing we identified it with, and rotate the particles so that the two axes of the packing align with the reference. Then, we simply obtain for each particle position $\mathbf{x}_i$ in the packing the particle position in the reference $\mathbf{x}_j(i)$ that is closest to it. The RMSD is then simply calculated as

$$\mathrm{RMSD} = \sqrt{\frac{1}{N}\sum_{i=1}^{N} \|\mathbf{x}_i - \mathbf{x}_j(i)\|^2}.$$

In Fig. S 7a we show the time trace of the RMSD and the fluctuations in the packing type for $N = 72$ Lennard-Jones particles at $T = 0.02\ \epsilon/k_B$. Note that the RMSD for the D_{5h} and D_3 packings are significantly lower than for the icosahedral packing, presumably due to the higher configurational entropy of the icosahedral packing. In Fig. S 7b we show another time trace of the

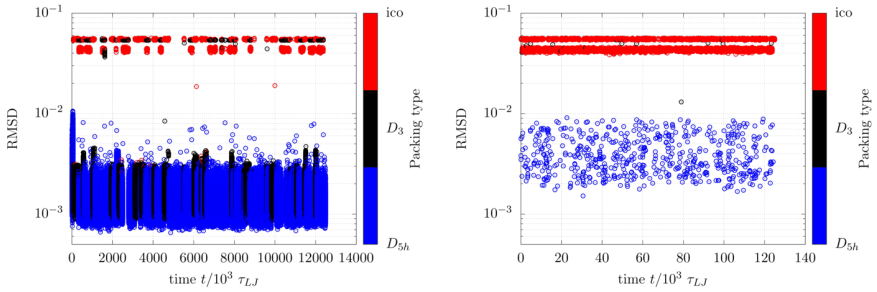

(a) (b)

Figure S 7: (Colour online.) Root mean square deviation from assumed packing type at $T = 0.02\ \epsilon/k_B$ (a) and $T = 0.066\ \epsilon/k_B$ (b). Note the different time scale needed for the lower temperature to sample a sufficient number of transitions between the packings.

RMSD, but now for $T = 0.066\ \epsilon/k_B$, which is close to the temperature used in Ref. (7). Note that in this case the dominant packing is the icosahedral one. The RMSD is higher for all packings due to larger thermal fluctuations. Note furthermore that the rearrangements from D_{5h} to icosahedral and back are much more frequent at the higher temperature.

For the lower temperatures of $T = 0.02\epsilon/k_B$ the average occupation fraction of the different states was still in the process of converging, as can be seen from figure S 8. Since the total sampling length for the temperatures $T \leq 0.03\epsilon/k_B$ was ten times longer, we see that increasing the temperature from $T = 0.02\epsilon/k_B$ to $T = 0.05\epsilon/k_B$ leads to convergence more than ten times as fast, from which it becomes clear that the frequency of rearrangements for Lennard-Jones packings increases very rapidly with temperature.

With the analysis described here, we can determine the packing for each frame, and from this we construct occurrence frequencies for each packing. Under the assumption that the simulations are ergodic, these can be converted into free energy differences, as explained in the main text.

For the Morse potential the above procedure is not viable at low temperatures, presumably because the energy barriers between the packings are much larger. To emphasise this, we show in Fig. S 9 the frequency of observed switches between the low energy packings per simulation time for $N = 72$ for

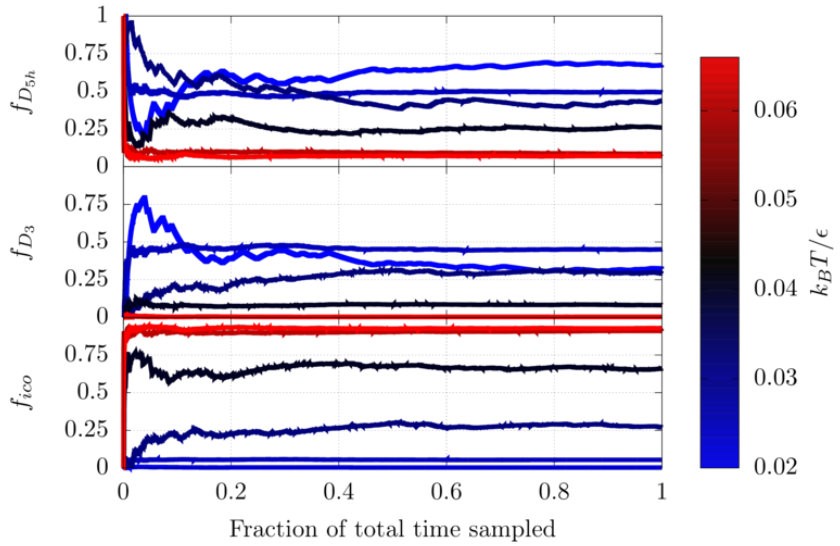

Figure S 8: Converging of the observed frequency of the different packings with the fraction of total time sampled. The lower temperatures $T \leq 0.03\epsilon/k_B$ had a total sample time ten times longer than that of the higher temperatures.

both the Lennard-Jones and Morse particles. The low energy packings are shown in Figs. 3 for Lennard-Jones and 9 for Morse. Note that the Lennard-Jones packing exhibits a maximum at around $T = 0.03\epsilon/k_B$. This is because at this point all three packings are roughly equally likely. The Morse packings only show significant rearrangements for $T > 0.75\ \epsilon/k_B$, even though the potential energy difference between the two packings is of a similar order as the potential energy difference between the Lennard-Jones D_{5h} and icosahedral packings ($\approx 1.6 \times 10^{-3}\epsilon$ for Lennard-Jones against $1.58 \times 10^{-3}\epsilon$ for Morse). This hints at a much larger kinetic barrier between the packings, and thus a simple sampling of the frequencies is not a viable approach to determine the free energy of the packings.

References

[1] Jeroen M. Voogd. *Crystallisation on a Sphere*. PhD thesis, Universiteit van Amsterdam, 1994.

[2] Kevin Q. Brown. Voronoi diagrams from convex hulls. *Information Processing*

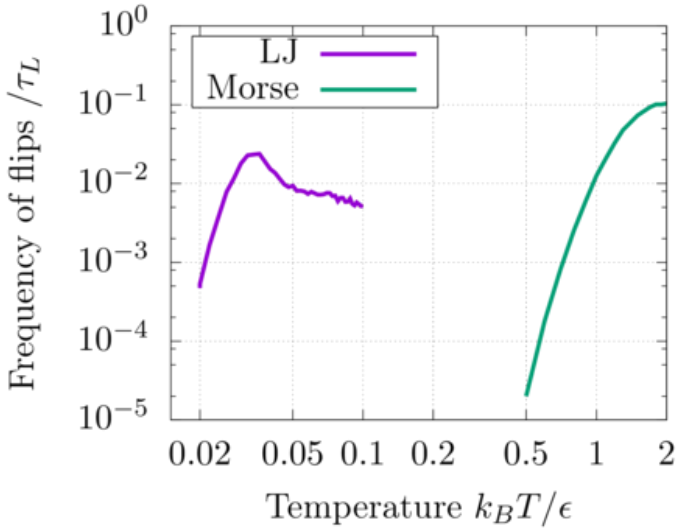

Figure S 9: (Colour online.) Observed frequency of switches between packings. Note that for the low temperatures, the Morse packing does not exhibit any switches at all in the sampled time.

Letters, 9:223–228, 1978.

[3] The CGAL Project. *CGAL User and Reference Manual*. CGAL Editorial Board, 4.7 edition, 2015.

[4] J. P. Troadec, A. Gervois, and L. Oger. Statistics of voronoi cells of slightly perturbed face-centered cubic and hexagonal close-packed lattices. *EPL (Europhysics Letters)*, 42(2):167, 1998.

[5] David J. Wales and Sidika Ulker. Structure and dynamics of spherical crystals characterized for the thomson problem. *Phys. Rev. B*, 74:212101, Dec 2006.

[6] David J. Wales, Hayley McKay, and Eric L. Altschuler. Defect motifs for spherical topologies. *Phys. Rev. B*, 79:224115, Jun 2009.

[7] Roya Zandi, David Reguera, Robijn F. Bruinsma, William M. Gelbart, and Joseph Rudnick. Origin of icosahedral symmetry in viruses. *PNAS*, 101(44):15556–15560, Nov 2004.

[8] David J. Wales. Gmin, 2015. Downloaded on August 20th, 2015 from `http://www-wales.ch.cam.ac.uk/GMIN/`.